Structure of the deep lithosphere between Pamir and Tarim

Wasja Bloch[1], Bernd Schurr[1], Xiaohui Yuan[1], Lothar Ratschbacher[2], Sanaa Reuter[2], Sofia-Katerina Kufner[1,3], Qiang Xu[4,5], and Junmeng Zhao[4,5]

[1]*GFZ German Research Centre for Geosciences, 14473 Potsdam, Germany*

[2]*Geologie, Technische Universität Bergakademie Freiberg, 09599 Freiberg, Germany*

[3]*British Antarctic Survey, Cambridge CB3 0ET, England*

[4]*Key Laboratory of Continental Collision and Plateau Uplift, Institute of Tibetan Plateau Research, Chinese Academy of Sciences, Beijing 100101, China*

[5] *CAS Center for Excellence in Tibetan Plateau Earth Sciences, Beijing 100101, China*

This manuscript is a non-peer reviewed preprint submitted to EarthArXiv.

It is under review in GEOLOGY (Geological Society of America)

ABSTRACT

The Pamir protrudes ~300-km between the Tajik and Tarim lithosphere of central Asia. It overlies a Wadati-Benioff earthquake zone connected to a low velocity zone interpreted as crustal rocks. Together with the mantle lithosphere it constitutes the arc-shaped Asian slab. We use new seismic data to better constrain the lithospheric architecture of the Pamir where it abuts the Tarim block and test competing models of its formation. With complemented local-seismicity and focal-mechanism catalogs and a P-wave velocity model that spans the Pamir and the western Tarim lithosphere, we infer the presence of a high velocity zone, interpreted as an Indian mantle lithosphere indenter, delaminating the Asian slab and overturning it in the eastern Pamir. The indenter bends down in the east under the northwestern Kunlun, where it terminates. The indenter–Tarim lithosphere interface is a compressive transform zone lined by a slice of Pamir Plateau crust. As the largest principal stress at depth parallels surface motion and both are highly oblique to the western Tarim margin, this crustal slice is likely dragged with the indenter and downward underneath the Tarim lithosphere.

INTRODUCTION

The Pamir—the northwestern prolongation of the Tibetan plateau—is bordered by the Tian Shan, the Tajik basin, and the Tarim basin, in the north, west, and east, respectively; the latter is a cratonic block (e.g., Lu et al., 2008). The northern Pamir and the Kunlun of northwestern Tibet comprise subduction-accretion-arc complexes accreted to and built on Asian continental basement. The central and southern Pamir and the Karakorum and Hindu Kush represent Gondwana-derived microcontinents and subduction-accretion-arc complexes (Fig. 1; Burtman and Molnar, 1993; Schwab et al., 2004). Beneath the Pamir, a band of intermediate-depth (50–250 km) earthquakes extends from the southwestern Pamir northwestward into the central Pamir, bends eastward, and shows diminished earthquake activity beneath the eastern Pamir (Fig. 2; Pegler and Das, 1998; Sippl et al., 2013a). Receiver function images, seismic tomography, and the analysis of guided waves show that the earthquakes in the western and central Pamir reside in a 10–15 km thick, E- to S-dipping low velocity zone (LVZ) connected to the Asian lithosphere; seismic velocities indicate that the LVZ represents continental crust, constituting together with the underlying mantle lithosphere the Asian slab (Schneider et al., 2013; Sippl et al., 2013b; Mechie et al., 2019). Beneath the northwestern Kunlun, diffuse seismicity at 100–150 km depth was attributed to Tarim lithosphere underthrusting the Pamir (Fan et al. 1994; Pegler and Das, 1998).

Whether Asian lithosphere subducts as a narrow, back-rolling slab of thinned crust (Burtman and Molnar, 1993; Sobel et al., 2013) or whether forceful subduction/delamination of lower crust and mantle lithosphere due to indentation by cratonic Indian mantle lithosphere (Kufner et al., 2016; Metzger et al., 2017) occurs is debated. This debate impacts on the understanding of processes like continental subduction, indentation, delamination, and rollback.

If an indenter governs the shape of the Pamir orocline, its margins matter. Kufner et al. (2018) argued that a sinistral-oblique transform margin separates indenting cratonic Indian lithosphere beneath the Pamir from subducting Indian continental-margin lithosphere below the Hindu Kush. The most recent subduction model (Sobel et al., 2013) calls for rollback of a narrow Asian slab with thinned continental crust, involving mantle corner flow and a subduction-transform edge propagator fault separating the subducting Asian slab and its hanging wall from the Tarim block. However, geophysical data indicate that the hinterland crust is not thinned (>50 km; Schneider et al., 2019). The delamination model (Kufner et al., 2016; Chapman et al., 2018) calls for forced Asian slab subduction due to flat-slab underthrusting of a mechanically-strong Indian continental lithospheric mantle indenter, a process recently modeled for the Pamir (Kelly and Beaumont, 2021). The indenter is imaged by refraction seismics and local body wave tomography as a high velocity zone (HVZ) south of the Asian slab (Mechie et al., 2012; Sippl et al., 2013b). Teleseismic body and surface wave tomography shows that it connects with the exposed Indian craton (e.g., Li et al., 2008; Liang et al., 2020); its northern extent has remained unresolved due to the smearing of the HVZ with cratonic Asia.

Herein, intermediate-depth earthquakes, focal-mechanism stress data, and a P-wave velocity model derived from new and published local seismological data illuminate the lithospheric configuration of the central and eastern Pamir and the boundary zone with Tarim. We characterize the northern tip of an indenter—interpreted as a promontory of Indian mantle lithosphere—and its eastern edge, where it abuts on the lithosphere of the Tarim block. We use seismograms recorded with two new local seismic networks (Yuan et al., 2018a; 2018b) and additional regional stations (PMP International, 2005; SEISDMC, 2021) to locate seismicity in the eastern Pamir jointly with an existing catalog from the western and central Pamir (Sippl et al., 2013b), and invert for the 3-dimensional subsurface P-wave velocity structure. The full description of the data and methods (Fig. S1; Fig. S2), the seismicity catalog, and the velocity structure are presented in the Supplemental Material.

SEISMICITY

Crustal seismicity of the upper 30 km is dominated by the aftershock sequences of strong earthquakes that struck the Pamir in 2015/16 and is omitted from the main figures. The middle and lower crust (30–50 km depth) is essentially aseismic (Fig. S3). Intermediate-depth earthquakes in the central and eastern Pamir outline three steeply-dipping, planar to curviplanar segments separated by regions of sparse seismicity (Fig. 2; Fig. 3).

Segment 1 begins at 72.8°E, 38°N, in continuation of the NE-striking, planar seismicity structure farther to the southwest (Fig. 2, Schneider et al., 2013; Sippl et al., 2013a). It forms a S- to SE-dipping band between 73°E and 74.3°E, and shows vigorous seismicity between 70–180-km-depth in its easternmost part (Fig. 3A; Fig. S2); farther east, seismic activity decreases.

Segment 2 in the eastern Pamir—in the direct continuation of segment 1—contains a few earthquakes at 50–80 km depth in a S-dipping structure (top dotted line in Fig. 3B). Below—at 80–170 km depth—the earthquake-defined band dips N (Fig 2; bottom dotted line in Fig. 3B). Seismicity in segment 2 is less intense compared to segment 1 (Fig. S2). Focal mechanisms of segments 1 and 2 indicate a transpressional stress regime, with the maximum principal stress σ_1 trending N20°W and N12°W, parallel to the surface plate-motion directions, and a vertical σ_3 (Fig. 2).

Seismicity in segment 3 forms a continuous, ~ENE-dipping structure at 80–120-km-depth between 37°N and 38°N; it follows the northwestern Kunlun (Fig. 2; Fig. 3C). Seismic activity is comparably weak (Fig. S2). Focal mechanisms indicate transpression with σ_1 trending N7°W, parallel to the surface plate-motion, and a down-dip σ_3 (Fig. 2).

VELOCITY STRUCTURE

In the shallow crust, northeast of the Main Pamir Thrust System (Fig. 3, overview map), the sediment fill of the Tarim basin forms a LVZ (<5 km/s, *TL* in Figs. 3B–D). In the middle–lower crust, the Tarim basement appears as a discontinuous HVZ (6.5–7.5 km/s, *TH* in Fig. 3C, Fig. 3E) at the poorly-resolved rim of the tomographic volume. A LVZ is located in the uppermost mantle of northwestern Tarim (*AL* in Fig. 3G). An arcuate crustal LVZ extends below the northern Pamir, the Kongur Extensional System, and the northwestern Kunlun (5–6 km/s, *PL* in Figs. 3A–C and 3E). It is sandwiched between the Tarim basement HVZ, *TH*, and another crustal HVZ in the central Pamir (6–7 km/s, *PH* in Fig. 3A; Fig. 3E).

At mantle depths, dipping LVZs are located above the seismicity in segments 1–3 (7–8 km/s, *L1*, *L2*, *L3* in Figs. 3A-C and 3F). The LVZs *L2* and *L3* of segments 2 and 3 appear continuous in map view (Fig. 3F), but are separated by the seismicity of segment 2 (Fig. 3B). The seismically active structures are underlain by HVZs (8.5–9.5 km/s, *H1, H2, H3* in Figs. 3A–C and 3G) and have the same dip as the LVZs above. In segment 1 and 2, the HVZs *H1* and *H2* are continuous along strike below ~105 km depth (Fig. 3G). In segment 2, the HVZs *H2* and *H3* touch, but are separated by seismicity in the same way as the LVZs *L2* and *L3* (Fig. 3B; Fig. 3G). The LVZs and HVZs of segment 1 (*L1* and *H1*; Fig. 3A) and segment 3 (*L3* and *H3*; Fig. 3C) dip in the same direction as the seismicity structures; those of segment 2 (*L2* and *H2*; Fig. 3B) dip oppositely.

INTERPRETATION AND DISCUSSION

We visualize our interpretation of the lithospheric architecture of the central and eastern Pamir in the block diagram of Figure 4. Sippl et al. (2013b) inferred eclogitization of the lower crust of segment 1 due to the sinking of the Asian slab and that this lower crust hosts the band of intermediate-depth earthquakes; in our tomogram, we interpret the LVZ *L1* as the lower crust and the HVZ *H1* as the mantle lithosphere of the Asian slab (Fig. 3A). The aseismic mid-crustal LVZ *PL* (Figs. 3A–C and 3E; see also Sippl et al., 2013b; Li et al., 2018), possibly connecting the upper crustal imbrication of the Main Pamir Thrust System with tectonic stacking along shear zones in the middle crust (Fig. 1, cross section), may represent a heated rock volume, developed by excess radiogenic heat production in the thickened crust. Heating due to asthenospheric inflow in the hanging wall of a S-dipping subduction zone is unlikely, as the tomogram does not show a LVZ south of the seismic zone; in contrast, subcrustal P velocities are >8km/s with HVZs (>8.5 km/s) embedded (e.g., *H3*), indicating relatively cold and rigid lithospheric mantle south of the Asian slab.

Segment 2 appears to be the eastern continuation of segment 1 of the Asian slab because of the similar depth extent of the seismic zone and the continuity of the underlying HVZ (Fig. 2; Figs. 3A, 3B, and 3G). The seismically active structure is overturned below ~80 km depth. A tear likely separates segments 1 and 2 because of the short (~40 km) distance across which the slab dip changes and the separating seismicity gap. The Asian slab terminates in a seismicity cluster below the Kashgar-Yecheng Transfer System at 76.2°E (Fig. 2), where it appears torn off Tarim's lithosphere to the east. The dip beyond vertical of segment 2 may be an indication of indentation, because rollback alone cannot steepen the slab to more than vertical (Magni et al., 2013).

For segments 1–3, σ_1 at depth is parallel to the ~NNW-oriented surface velocity of the Pamir crust (e.g., Zubovich et al. 2010, Ischuk et al., 2013, Metzger et al., 2020). The subhorizontal σ_1 indicates that a NNW–SSE compressive stress field governs the deep structure of the Pamir, which favors a pushing indenter. In contrast, N–S extension should occur S of the slab if deformation below the Pamir was governed by a narrow Asian slab rolling back northward. Parallelism of the surface motion with σ_1 at depth implies that the lithospheric mantle is coupled to the crust. For segments 1 and 2 it arises if collision occurs at an indenter tip.

In concert with the lack of thinned hinterland crust and the imaging of a HVZ at ~200 km depth below the Pamir-Karakorum that connects with the exposed Indian craton, the following of our observations support the presence of an indenter below the Pamir: (1) the repeated detection of HVZ *H3* south of the Asian slab (Mechie et al., 2012; Sippl et al., 2013b; this study) that excludes asthenospheric inflow above a S-dipping, back-rolling subduction zone; (2) the overturned dip of the seismic plane of segment 2; (3) the NNW–SSE compressive stress field across the central and eastern Pamir at mantle depth that is coupled with surface motion.

The indenter is most likely cratonic Indian lithosphere, because the lithosphere of the central and southern Pamir terranes would be too weak to transmit enough force to delaminate and overturn the Asian slab (Kelly and Beaumont, 2021). We locate the delamination front at the base of the rheological weak mid-crustal LVZ *PL* (red line in Fig. 4). The present location and form of the Pamir and the Asian slab is in this interpretation governed by the shape of the indenter. Additional structural complexity, such as the location of slab tears or turn-overs, may be due to lateral changes in the strength of the indented Asian lithosphere or the along-strike variability of the indenter tip (Li et al., 2016; Kelly and Beaumont, 2021). For example, the mid-crustal HVZ *PH*, which overlies a distinctive Moho bulge in segment 1 (Fig. 3A; Schneider et al., 2019), may represent a lithosphere-scale anticline; in segment 1, the top of the indenter appears to rise higher than in segment 2 and in particular in segment 3 (Fig. 4).

In the northwestern Kunlun, the seismicity band of segment 3, the LVZ *L3*, and the HVZ *H3* dip ~ENE, indicating that Pamir crust and indenter mantle lithosphere underthrusts the Asian mantle lithosphere (Fig. 3C). The earthquakes may occur in thickened crust undergoing eclogitization. This crust is dragged to depth between the bulldozing indenter and the margin of the Tarim block. The underthrusting interpretation is supported by a doubled ~E-dipping Moho (Xu et al., 2021). The stress field of the earthquakes inside the underthrusting crust *L3* indicates that it moves with the NNW-ward moving indenter. The orientation of σ_1 in segment 3 testifies that underthrusting is highly oblique with respect to Tarim hanging wall. As the tomographic and receiver function Moho both dip ~WSW beneath the northwestern Kunlun east of LVZ *L3* (Fig. 3C; Xu et al., 2021), we infer that Tarim underthrusts the northwestern Kunlun as well, building a stack of Pamir and Kunlun–Tarim crust (Fig. 4C). This excess crust may be responsible for a positive anomaly in the isostatic gravity residual (Balmino et al., 2012; 20-mGal-contour in Fig. 2) that flanks the northern edge of the Tibet plateau (Fig. 2, inset), and was interpreted to represent thrusting of Tarim crust under the western and central Kunlun (Wittlinger et al., 2004).

The transpressive stress field of the deep seismic zone (segment 3) outlines a compressive lithospheric transform zone as the deep plate boundary between the Indian indenter and the Tarim block. It changes to a forced subduction/delamination boundary due to indentation under the central Pamir. The tear that separates the Asian slab from Tarim propagates northward with the advancing indenter. Indentation may have caused the capture and dragging along of the crust from the collision system into the transform zone (Fig. 4C). The transform margin likely transitions southeastward into a subduction plate boundary where the Tarim block underthrusts the western Tibet plateau. Our interpretation of the deep structure suggests a strong along-strike segmentation of the northern tip of the Indian plate; it subducts under the Hindu Kush (Kufner et al., 2021), indents in the Pamir (this study), and has variable dip angles and locations in the rest of Tibet (e.g., Zhao et al., 2011).

CONCLUSION

We located zones of intermediate-depth seismicity in the eastern Pamir and northwestern Kunlun, established their geometries, determined the principal stress orientations, and computed a seismic velocity model of the subsurface. We traced a subducting/delaminating Asian slab eastward as far as the western edge of the Tarim block and showed that the eastern segment of the slab is overturned and torn from the central one. Together with the presence of a high velocity zone in front of the slab and the parallelism of the largest principal stress at depth with surface motion across the eastern and central Pamir, this geometry indicates underthrusting of Indian mantle lithosphere beneath the Pamir and delamination of the Asian slab. A slice of lower crust is dragged along with the indenter and smeared into the compressive transform boundary with the Tarim block at depth.

ACKNOWLEDGMENTS

We thank the drivers and field participants from the Institute of Tibetan Plateau Research, especially Hongbing Liu, who helped to organize the station deployment, and Christian Sippl for sharing code and discussion. Funded by the CaTeNA project of the German Federal Ministry of Science and Education (support codes 03G0878A and 03G0878B). Seismic data was handled using *obspy* (Krischer et al., 2015). Part of the instruments were provided by GIPP of GFZ Potsdam. Seismic data are archived by GEOFON data center.

Figure 1: Tectonic units of the Pamir in map view and as a schematic cross section along ~74°E. MPTS: Main Pamir Thrust System; KYTS: Kashgar-Yecheng Transfer System; KES: Kongur Extensional System.

Figure 2: Seismotectonic map of the Pamir and northwestern Kunlun with seismic networks, seismicity, focal mechanisms, principal stress directions, earthquake P-, T-, N-axes, global navigation satellite system (GNSS) velocity field (Zubovich et al., 2010; Ischuk et al., 2013), and 20mGal positive isostatic gravity anomaly (Balmino et al., 2012). TJS, Tanymas-Jinsha suture.

Figure 3: Sections through the tomogram. A-C) Profiles shown on overview map. Magenta: Receiver function Moho (Schneider et al., 2019; Xu et al., 2021). D-G) Horizontal sections. TH, PH, H1, H2, H3: high velocity zones. TL, PL, L1, L2, L3, AL: low velocity zones.

Figure 4: Top: pre-collision geometry. Bottom: interpreted block diagram of the deep lithospheric structure beneath the Pamir and northwestern Kunlun. A-C) Interpreted cross sections of Fig. 3. '///' symbols mark the lower crust involved in the collision process.

REFERENCES CITED

Balmino, G., Vales, N., Bonvalot, S., and Briais, A., 2012, Spherical harmonic modeling to ultra-high degree of Bouguer and isostatic anomalies: Journal of Geodesy, v. 86, p. 499–520, doi:10.1007/s00190-011-0533-4.

Burtman, V. S., and Molnar, P. H., 1993, Geological and geophysical evidence for deep subduction of continental crust beneath the Pamir: Geological Society of America, Special Papers, v. 281, p. 1-76.

Chapman, J. B., Carrapa, B., Ballato, P., DeCelles, P. G. , Worthington, J., Oimahmadov, I., Gadoev, M., and Ketcham, R., 2017, Intracontinental subduction beneath the Pamir Mountains: Constraints from thermokinematic modeling of shortening in the Tajik fold-and-thrust belt: Geological Society of America Bulletin, v. 129, p. 1450–1471, doi:10.1130/B31730.1.

Fan, G., Ni, J. F., and Wallace, T. C., 1994, Active tectonics of the Pamirs and Karakorum: Journal of Geophysical Research: Solid Earth, v. 99, p. 7131–7160. doi:10.1029/93JB02970.

Ischuk, A., Bendick, R., Rybin, A., Molnar, P., Khan, S. F., Kuzikov, S., Mohadjer, S., Saydullaev, U., Ilyasova, Z., Schelochkov, G., et al., 2013, Kinematics of the Pamir and Hindu Kush regions from GPS geodesy: Journal of Geophysical Research: Solid Earth, v. 118, p. 2408–2416. doi:10.1002/jgrb.50185.

Kelly, S., and Beaumont, C., 2021, Balanced cross-sections and numerical modelling of the lithospheric-scale evolution of the Hindu Kush and Pamir: Journal of Geophysical Research: Solid Earth, e2020JB020678. doi:10.1029/2020JB020678.

Krischer, L., Megies, T., Barsch, R., Beyreuther, M., Lecocq, T., Caudron, C., and

Wassermann, J., 2015, ObsPy: A bridge for seismology into the scientific Python ecosystem: Computational Science & Discovery, v. 8, p. 14003. doi:10.1088/1749-4699/8/1/014003.

Kufner, S.-K., Schurr, B., Sippl, C., Yuan, X., Ratschbacher, L., Ischuk, A., Murodkulov, S., Schneider, F., Mechie, J., Tilmann, F., et al., 2016, Deep India meets deep Asia: Lithospheric indentation, delamination and break-off under Pamir and Hindu Kush (Central Asia). Earth and Planetary Science Letters, v. 435, p. 171–184, doi:10.1016/j.epsl.2015.11.046.

Kufner, S.-K., Schurr, B., Ratschbacher, L., Murodkulov, S., Abdulhameed, S., Ischuk, A., Metzger, S. and Kakar, N., 2018, Seismotectonics of the Tajik basin and surrounding mountain ranges: Tectonics, 37, 2404–2424. doi:10.1029/2017TC004812.

Kufner, S.-K., Kakar, N., Bezada, M., Bloch, W., Metzger, S., Yuan, X., Mechie, J., Ratschbacher, L., Murodkulov, S., Deng, Z., and Schurr, B., 2021, The Hindu Kush slab break-off as revealed by deep structure and crustal deformation: Nature Communications. doi:10.1038/s41467-021-21760-w.

Li, C., Van der Hilst, R. D., Meltzer, A. S., and Engdahl, E. R., 2008, Subduction of the Indian lithosphere beneath the Tibetan Plateau and Burma: Earth and Planetary Science Letters, v. 274, p. 157–168, doi:10.1016/j.epsl.2008.07.016.

Li, Z.-H., Liu, M., and Gerya, T., 2016, Lithosphere delamination in continental collisional orogens: A systematic numerical study: Journal of Geophysical Research: Solid Earth, v. 121, p. 5186–5211, doi:10.1002/2016JB013106.

Li, W., Chen, Y., Yuan, X., Schurr, B., Mechie, J., Oimahmadov, I., and Fu, B., 2018, Continental lithospheric subduction and intermediate-depth seismicity: Constraints from S-wave velocity structures in the Pamir and Hindu Kush: Earth and Planetary Science Letters, v. 482, p. 478–489, doi:10.1016/j.epsl.2017.11.031.

Liang, Y., Li, L., Liao, J., and Gao, R., 2020, Interaction of the Indian and Asian plates under the Pamir and Hindu-Kush regions: Insights from 3-D shear wave velocity and anisotropic structures: Geochemistry, Geophysics, Geosystems, v. 21, e2020GC009041, doi:10.1029/2020GC009041.

Lu, S., Li, H., Zhang, C., and Niu, G., 2008, Geological and geochronological evidence for the Precambrian evolution of the Tarim Craton and surrounding continental fragments: Precambrian Research, v. 160, p. 94–107, doi:10.1016/j.precamres.2007.04.025.

Magni, V., Faccenna, C., van Hunen, J., and Funiciello, F., 2013, Delamination vs. break-off: the fate of continental collision: Geophysical Research Letters, v. 40, p. 285–289. doi:10.1002/grl.50090.

Mechie, J., Schurr, B., Yuan, X., Schneider, F., Sippl, C., Minaev, V., Gadoev, M., Oimahmadov, I., Abdybachaev, U., Moldobekov, B., et al., 2019, Observations of guided waves from the Pamir seismic zone provide additional evidence for the existence of subducted continental lower crust: Tectonophysics, v. 762, p. 1–16, doi:10.1016/j.tecto.2019.04.007.

Mechie, J., Yuan, X., Schurr, B., Schneider, F., Sippl, C., Ratschbacher, L., Minaev, V., Gadoev, M., Oimahmadov, I., Abdybachaev, U., et al., 2012, Crustal and uppermost mantle velocity structure along a profile across the Pamir and southern Tien Shan as derived from project TIPAGE wide-angle seismic data: Geophysical Journal International, v. 188, p. 385–407. doi:10.1111/j.1365-246X.2011.05278.x.

Metzger, S., Schurr, B., Ratschbacher, L., Sudhaus, H., Kufner, S.-K., Schöne, T., Zhang, Y., Perry, M., and Bendick, R., 2017, The 2015 Mw7. 2 Sarez strike-slip earthquake in the

Pamir interior: Response to the underthrusting of India’s western promontory: Tectonics, v. 36, p. 2407–2421. doi:10.1002/2017TC004581.

Metzger, S., Ischuk, A., Deng, Z., Ratschbacher, L., Perry, M., Kufner, S.-K., Bendick, R., and Moreno, M., 2020, Dense GNSS profiles across the northwestern tip of the India-Asia collision zone: Triggered slip and westward flow of the Peter the First Range, Pamir, into the Tajik Depression. Tectonics, v. 39, e2019TC005797. doi:10.1029/2019TC005797.

Pegler, G., and Das, S., 1998, An enhanced image of the Pamir–Hindu Kush seismic zone from relocated earthquake hypocentres: Geophysical Journal International, v. 134, p. 573–595, doi:10.1046/j.1365-246x.1998.00582.x.

PMP International (Tajikistan), 2005, Tajikistan National Seismic Network. International Federation of Digital Seismograph Networks. doi:10.7914/SN/TJ.

Schneider, F., Yuan, X., Schurr, B., Mechie, J. Sippl, C., Haberland, C., Minaev, V., Oimahmadov, I., Gadoev, M., Radjabov, N., et al., 2013, Seismic imaging of subducting continental lower crust beneath the Pamir: Earth and Planetary Science Letters, v. 375, p. 101–112, doi:10.1016/j.epsl.2013.05.015.

Schneider, F., Yuan, X., Schurr, B., Mechie, J., Sippl, C., Kufner, S.-K., Ratschbacher, L., Tilmann, F., Oimahmadov, I. Gadoev, M., et al., 2019, The crust in the Pamir: Insights from receiver functions: Journal of Geophysical Research: Solid Earth, v. 124, p. 9313–9331, doi:10.1029/2019JB017765

Schwab, M., Ratschbacher, L., Siebel, W., McWilliams, M., Minaev, V., Lutkov, V., Chen, F. Stanek, K., Nelson, B., Frisch, W., et al., 2004, Assembly of the Pamirs: Age and origin of magmatic belts from the southern Tien Shan to the southern Pamirs and their relation to Tibet: Tectonics, v. 23, TC4002, doi:10.1029/2003TC001583.

SEISDMC, 2021, Data management centre of the China National Seismic Network at the Institute of Geophysics, China Earthquake Administration, doi:10.11998/SeisDmc/SN, (http://www.seisdmc.ac.cn/)

Sippl, C., Schurr, B., Yuan, X., Mechie, J., Schneider, F., Gadoev, M., Orunbaev, S., Oimahmadov, I., Haberland, C., Abdybachaev, U. et al., 2013a, Geometry of the Pamir-Hindu Kush intermediate-depth earthquake zone from local seismic data: Journal of Geophysical Research. Solid Earth, v. 118, p. 1438–1457, doi:10.1002/jgrb.50128.

Sippl, C., Schurr, B., Tympel, J., Angiboust, S., Mechie, J., Yuan, X., Schneider, F., Sobolev, S. V., Ratschbacher, L., Haberland, C., et al., 2013b, Deep burial of Asian continental crust beneath the Pamir imaged with local earthquake tomography: Earth and Planetary Science Letters, v. 384, p. 165–177, doi:10.1016/j.epsl.2013.10.013.

Sobel, E. R., Chen, J., Schoenbohm, L. M., Thiede, R., Stockli, D. F., Sudo, M., and Strecker, M. R., 2013, Oceanic-style subduction controls late Cenozoic deformation of the Northern Pamir orogen: Earth and Planetary Science Letters, v. 363, p. 204–218, doi:10.1016/j.epsl.2012.12.009.

Wittlinger, G., Vergne, J., Tapponnier, P, Farra, V., Poupinet, G., Jiang, M. Su, H., Herquel, G. and Paul, A., 2004, Teleseismic imaging of subducting lithosphere and Moho offsets beneath western Tibet: Earth and Planetary Science Letters, v. 221, p. 117–130. doi:10.1016/S0012-821X(03)00723-4.

Xu, Q., Zhao, J., Yuan, X., Liu, H., Ju, C., Schurr, B. and Bloch, W., 2021, Deep crustal contact between the Pamir and Tarim Basin deduced from receiver functions: Preprint on https://essoar.org. doi:10.1002/essoar.10506378.1.

Yuan, X., Schurr, B., Bloch, W., Xu, Q., and Zhao, J., 2018a, East Pamir network, GFZ Data

Services, doi:10.14470/3U7560589977.

Yuan, X., B. Schurr, Kufner, S.-K., and Bloch, W., 2018b, Sarez Pamir aftershock seismic network, GFZ Data Services. doi:10.14470/4U7561589984.

Zhao, J., Yuan, X., Liu, H., Kumar, P., Pei, S., Kind, R., Zhang, Z., Teng, J., Ding, L., Gao, X., and others, 2010, The boundary between the Indian and Asian tectonic plates below Tibet: Proceedings of the National Academy of Sciences, v.107, p.11229–11233. doi:10.1073/pnas.1001921107.

Zubovich, A. V., Wang, X.-Q., Scherba, Y. G., Schelochkov, G. G., Reilinger, R., Reigber, C., Mosienko, O. I., Molnar, P., Michajljow, W., Makarov, V. I., et al., 2010, GPS velocity field for the Tien Shan and surrounding regions: Tectonics, v. 29, doi:10.1029/2010TC002772.

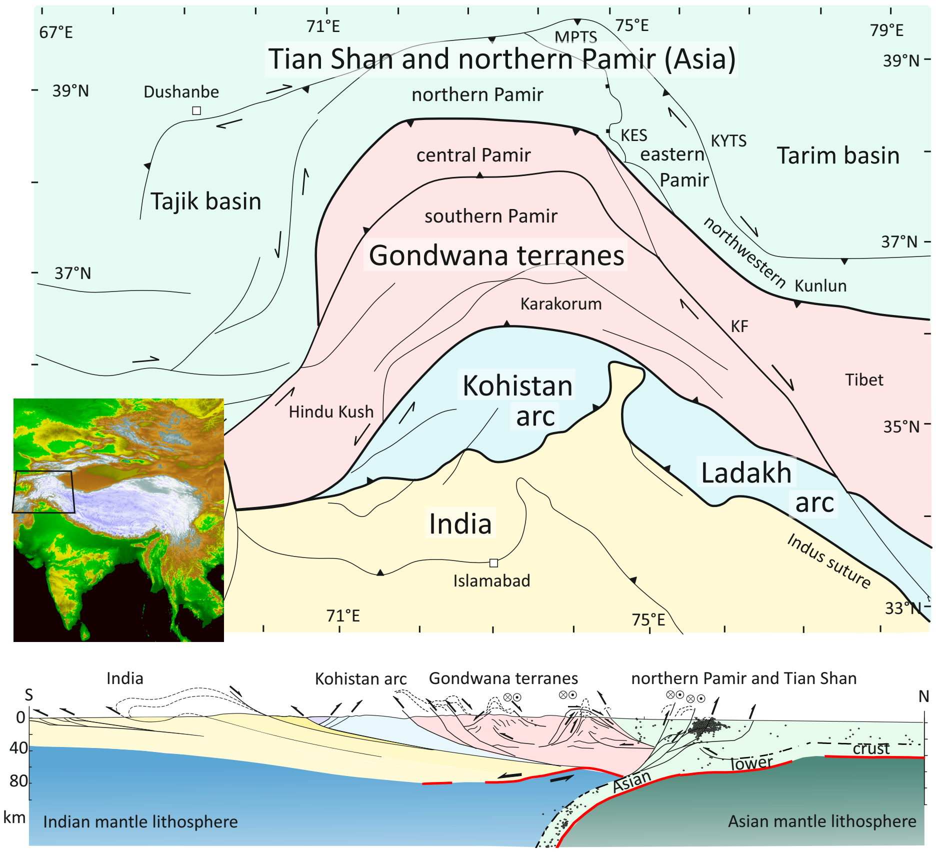

67°E
71°E
75°E
79°E
39°N
37°N
35°N
33°N
MPTS
Tian Shan and northern Pamir (Asia)
Dushanbe
northern Pamir
KES
KYTS
Tarim basin
central Pamir
eastern Pamir
Tajik basin
southern Pamir
northwestern Kunlun
Gondwana terranes
Karakorum
KF
Tibet
Kohistan arc
Hindu Kush
Ladakh arc
India
Islamabad
Indus suture
S
N
India
Kohistan arc
Gondwana terranes
northern Pamir and Tian Shan
0
40
80
km
Asian lower crust
Indian mantle lithosphere
Asian mantle lithosphere

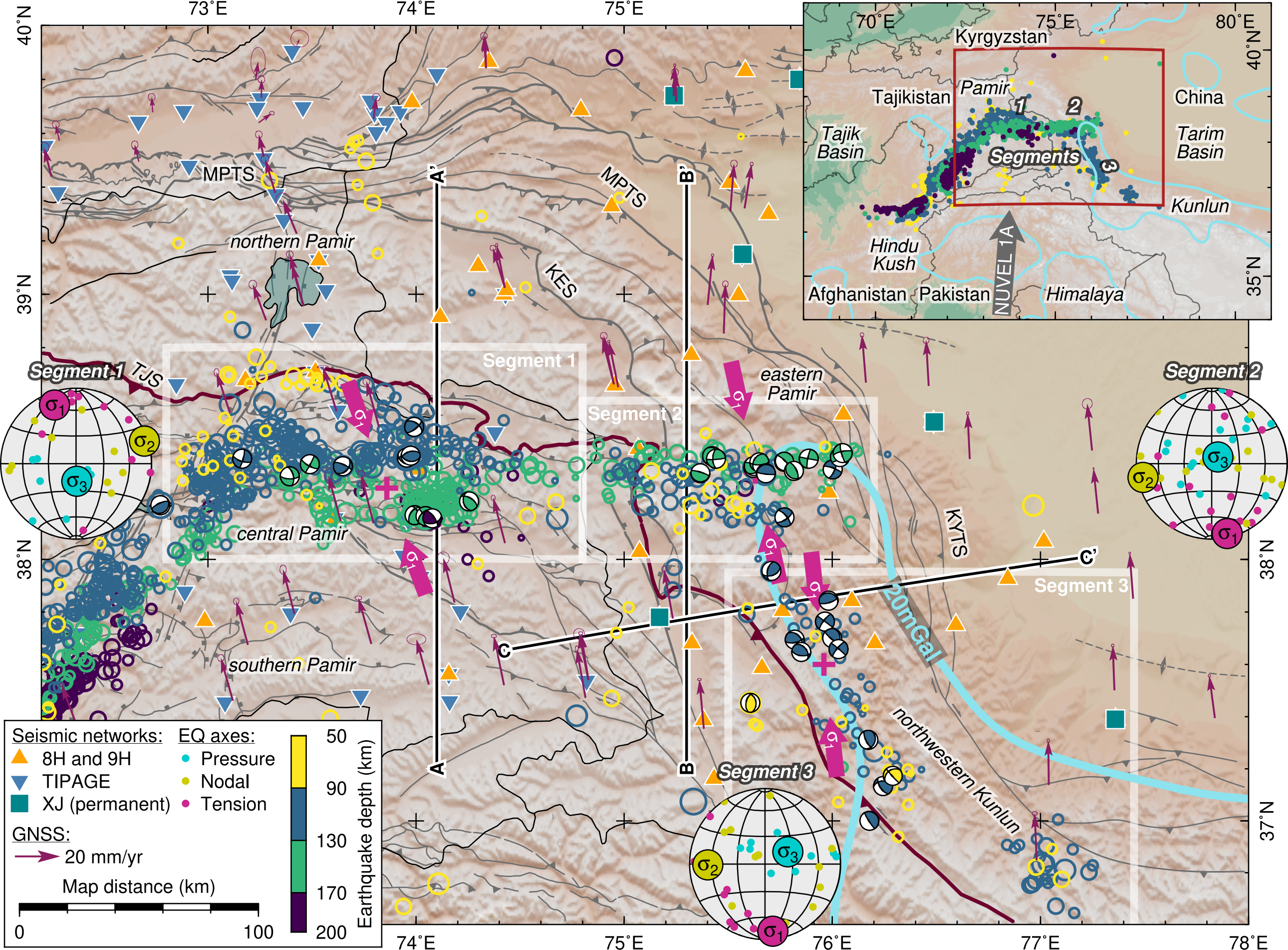

73˚E
74˚E
75˚E
76˚E
77˚E
78˚E
40˚N
39˚N
38˚N
37˚N
MPTS
northern Pamir
KES
eastern Pamir
Segment 1
Segment 2
Segment 3
TJS
central Pamir
southern Pamir
KYTS
20mGal
northwestern Kunlun
A
A'
B
B'
C
C'
σ1
σ2
σ3
70˚E
75˚E
80˚E
Kyrgyzstan
Tajikistan
Pamir
China
Tajik Basin
Tarim Basin
Segments
Kunlun
Hindu Kush
Afghanistan
Pakistan
Himalaya
NUVEL 1A
1
2
3
Seismic networks:
8H and 9H
TIPAGE
XJ (permanent)
EQ axes:
Pressure
Nodal
Tension
GNSS:
20 mm/yr
Map distance (km)
0
100
Earthquake depth (km)
50
90
130
170
200

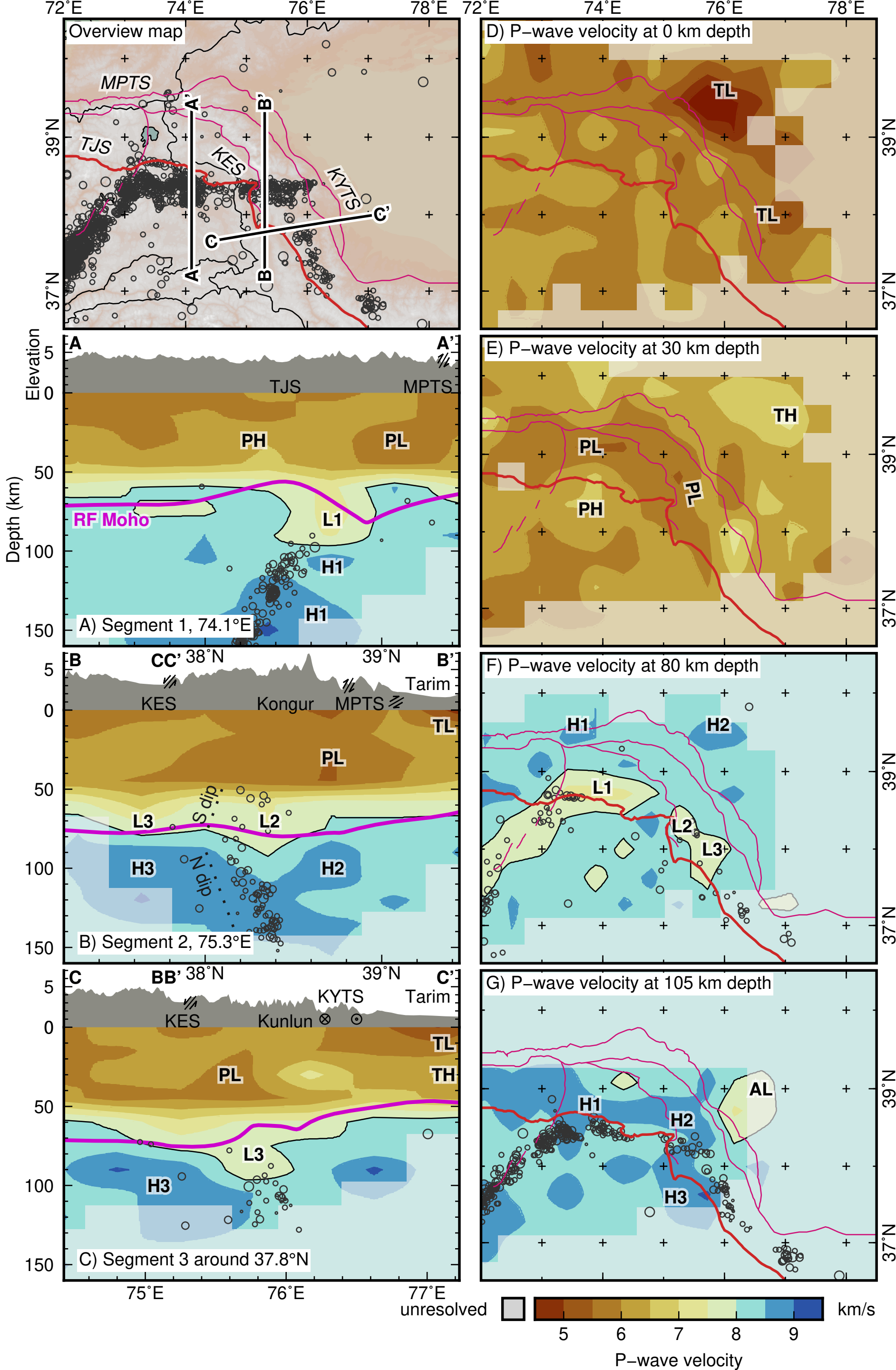

Overview map
MPTS
TJS
KES
KYTS
A
A'
B
B'
C
C'
72°E
74°E
76°E
78°E
39°N
37°N
D) P−wave velocity at 0 km depth
TL
TL
E) P−wave velocity at 30 km depth
TH
PL
PL
PH
F) P−wave velocity at 80 km depth
H1
H2
L1
L2
L3
G) P−wave velocity at 105 km depth
H1
H2
H3
AL
Elevation
Depth (km)
TJS
MPTS
PH
PL
RF Moho
L1
H1
H1
A) Segment 1, 74.1°E
CC'
38°N
39°N
KES
Kongur
MPTS
Tarim
TL
PL
S dip
N dip
L3
L2
H3
H2
B) Segment 2, 75.3°E
BB'
KES
KYTS
Kunlun
Tarim
TL
TH
PL
L3
H3
C) Segment 3 around 37.8°N
75°E
76°E
77°E
unresolved
km/s
5
6
7
8
9
P−wave velocity

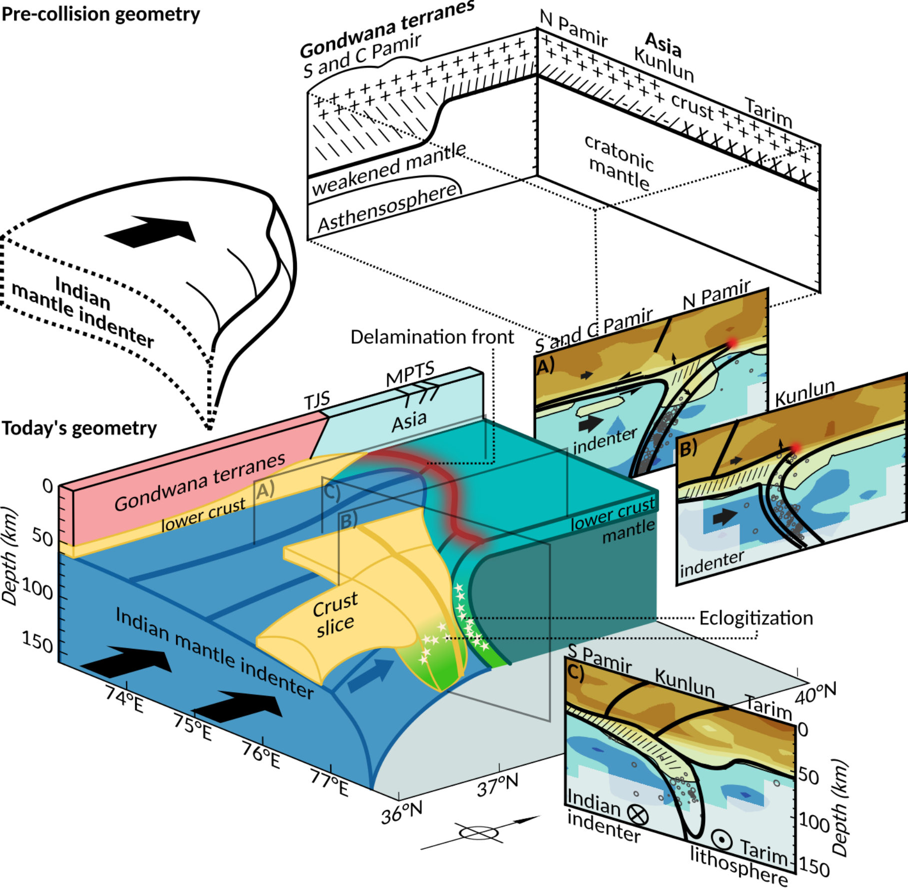
Pre-collision geometry
Gondwana terranes
S and C Pamir
N Pamir
Asia
Kunlun
crust
Tarim
weakened mantle
cratonic mantle
Asthensosphere
Indian mantle indenter
Delamination front
Today's geometry
TJS
MPTS
Asia
Gondwana terranes
lower crust
A)
B)
C)
Crust slice
lower crust
mantle
Eclogitization
Indian mantle indenter
Depth (km)
0
50
100
150
74°E
75°E
76°E
77°E
36°N
37°N
40°N
S and C Pamir
N Pamir
A)
indenter
Kunlun
B)
indenter
S Pamir
Kunlun
Tarim
C)
Indian indenter
Tarim lithosphere
0
50
100
150
Depth (km)

Supplement to

Structure of the deep lithosphere between Pamir and Tarim

Wasja Bloch[1], Bernd Schurr[1], Xiaohui Yuan[1], Lothar Ratschbacher[2], Sanaa Reuter[2], Sofia-Katerina Kufner[1,3], Qiang Xu[4], and Junmeng Zhao[4]

[1]*GFZ German Research Centre for Geosciences, 14473 Potsdam, Germany*

[2]*Geologie, Technische Universität Bergakademie Freiberg, 09599 Freiberg, Germany*

[3]*British Antarctic Survey, Cambridge CB3 0ET, England*

[4]*Institute of Tibetan Plateau Research, Chinese Academy of Sciences, Beijing 100085, China*

METHOD

Data

We operated the East Pamir seismic network (FDSN code 8H, Yuan et al., 2018a) with 30 sites in the eastern Pamir, northwestern Kunlun, and northwestern Tarim basin between August 2015 and July 2017, and the Sarez-Pamir aftershock seismic network (FDSN code 9H, Yuan et al., 2018b) with 10 sites in the central Pamir between February 2016 and July 2017. We used additional seismic waveform data from the Xinjiang regional seismic network (XJ, SEISDMC, 2021) and the Tajik National Seismic Network (FDSN network code TJ; PMP International, 2005; Fig. 2).

Seismic Event Detection, Phase Picking, and Initial Localization

We detected 39,309 seismic events using the *Lassie* earthquake detector (Comino et al. 2017), 10,900 of which at intermediate depth (>50 km), and automatically picked P-wave arrival times with *MannekenPix* (Aldersons, 2004) and S-wave arrival times with *spicker* (Diehl et al., 2009). After each arrival time picking run, events were located with *hypo71* (Lee and Lahr, 1972), and picks with the highest residuals were removed subsequently until the location root-mean-square misfit fell below a threshold of 2-s for P-waves only and 3-s for P- and S-waves combined. We then used a subset of 1,855 seismic events with best constrained arrival-time picks to invert for a depth-dependent 1-D velocity model and static station corrections using *velest* (Kissling et al., 1994). We again relocated all events in this model and removed those arrival times that yielded a residual 5 times larger than the standard deviation of all residuals of a certain seismic phase on a certain station. In total, we located 29,795 seismic events in the crust and in the mantle.

Inversion for the Subsurface Velocity Field

To derive a dataset suitable for tomographic inversion we augmented the catalog with events from Sippl et al. (2013b) and used a spatially declustered set of 2.264 events from the combined catalog with a total of 38.423 well-constrained P- and 15.910 S-arrival times. Inversion for the 3-D subsurface P-wave velocity structure was conducted using *simulps* (Thurber, 1983).

The seismic velocity field was parameterized as gradients between a rectangular grid of fixed nodes. After testing of various node configurations, we used a node spacing of 40-km in horizontal and 15-km in vertical direction (Figs. S1a and S3). The 1-D starting model was found by first inverting for the 1-D velocity gradients between vertical nodes and station corrections. Then, we constrained the velocities to increase with depth and that they do not exceed the velocity at 75-km depth (Fig. S1a). The model space was explored with various damping parameters (Fig. S1b) and the final model was found by first inverting solely for the velocity structure and earthquake parameters, and then allowing for minor adjustments by letting non-modeled residuals be taken up by station corrections. A checkerboard resolution test was used to assess the sensitivity of the model and mask poorly resolved regions (Fig. S3).

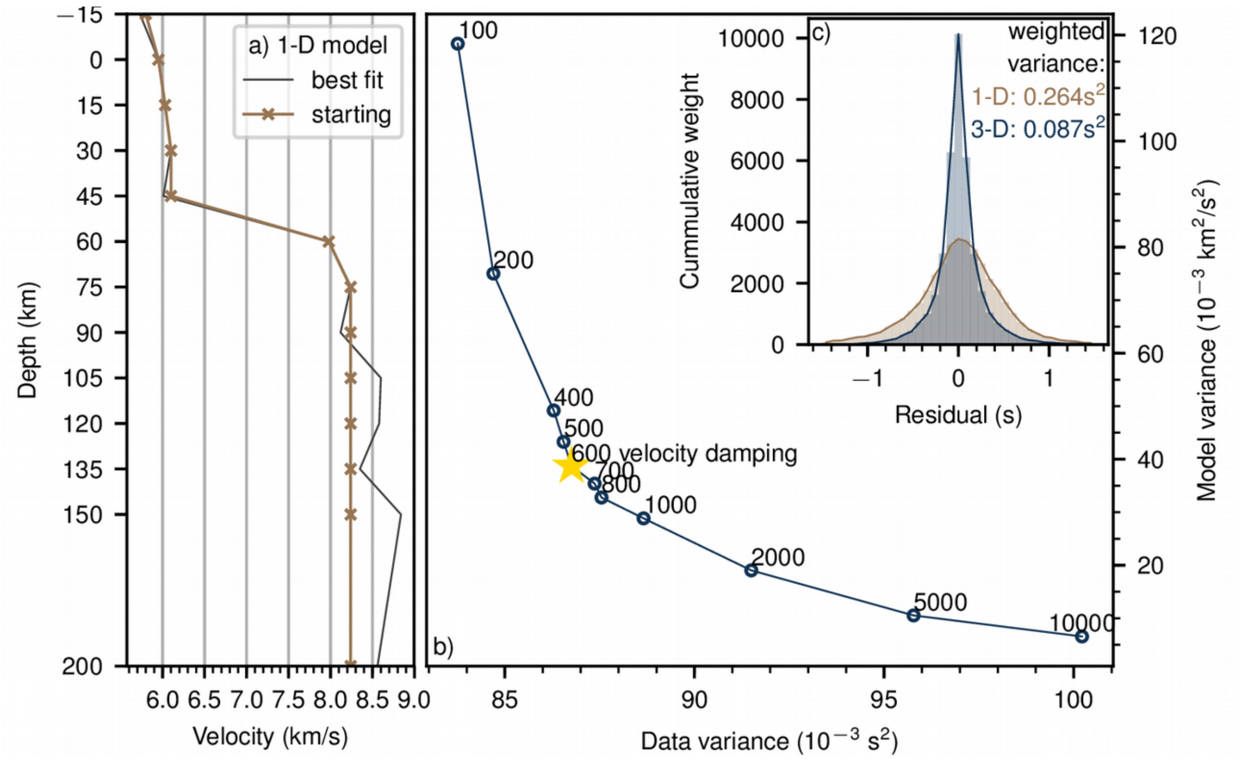

Figure S1: a) 1D models. Best fit: Minimum misfit model after 1-D inversion with simulps with station corrections. Starting: Starting model for the 3D inversion. We applied a positivity and a maximum velocity constraint to avoid pre-defining such essential structures in the 3-D inversion b) L-curve to find optimal velocity damping parameter. Star: chosen value c) Reduction of arrival time residuals and variance from 1-D starting model to the presented 3-D model.

Relocalization

To focus on sub-crustal processes we discarded crustal earthquakes (<50-km depth), which were dominated by a strong earthquake sequence and are confined to the upper ~40-km depth. We added intermediate depth earthquakes with at least 4 S-picks that were previously excluded from the tomographic inversion. We then relocated all events with the *hypoDD* algorithm (Waldhauser and Ellsworth, 2000), yielding a unified catalog of 1.493 events at intermediate depth, consisting of newly detected events in the eastern and central Pamir and previously reported events from the western and central Pamir (Sippl et al, 2013b).

Focal Mechanisms and Stress Directions

For 30 events, we estimated focal mechanisms using P-wave first motion polarities and P-to-S amplitude ratios using the *HASH* algorithm (Hardebeck and Shearer, 2003), and added 9 moment tensors of Kufner et al., (2016). For the three spatially clearly separated seismicity segments we inverted for the principal stress directions using the *slick* algorithm (Gephart and Forsyth, 1984).

PROPERTIES OF SEISMICITY

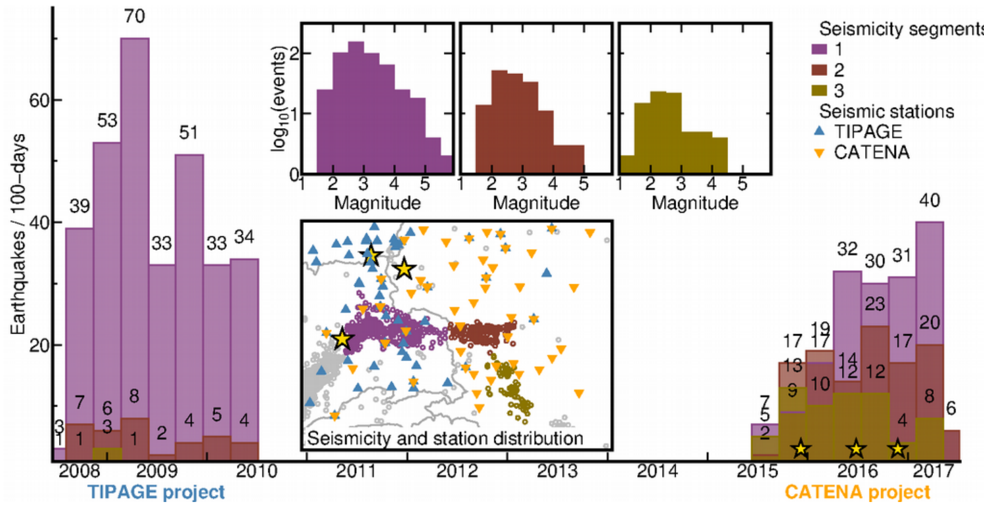

Figure S2: Seismicity rate, local event magnitudes, and station distribution for the three seismicity segments discussed in the main article. Stations of the TIPAGE project (2008-2010, blue) were located in the Tajik Pamir and covered the central segment. Stations of the CATENA project (2015-2017, orange), including networks 8H, 9H and XJ, were located in the Chinese Pamir and Tarim basin and covered the eastern and south-eastern segment. Additional stations were placed in the Tajik Pamir in February 2016. Aftershock sequences of strong earthquakes (stars) in December 2015, June 2016, and November 2016 represent seismic noise that lowered the detection capability of intermediate depth seismicity. Magnitudes of events that occur outside one of the networks (especially in the south-eastern segment) tend to be overestimated. Event rate in the central segment is significantly higher compared to the eastern and south-eastern segment, despite the different network configuration and noise conditions.

COMPLE SEISMIC TOMOGRAPHY RESULTS

127

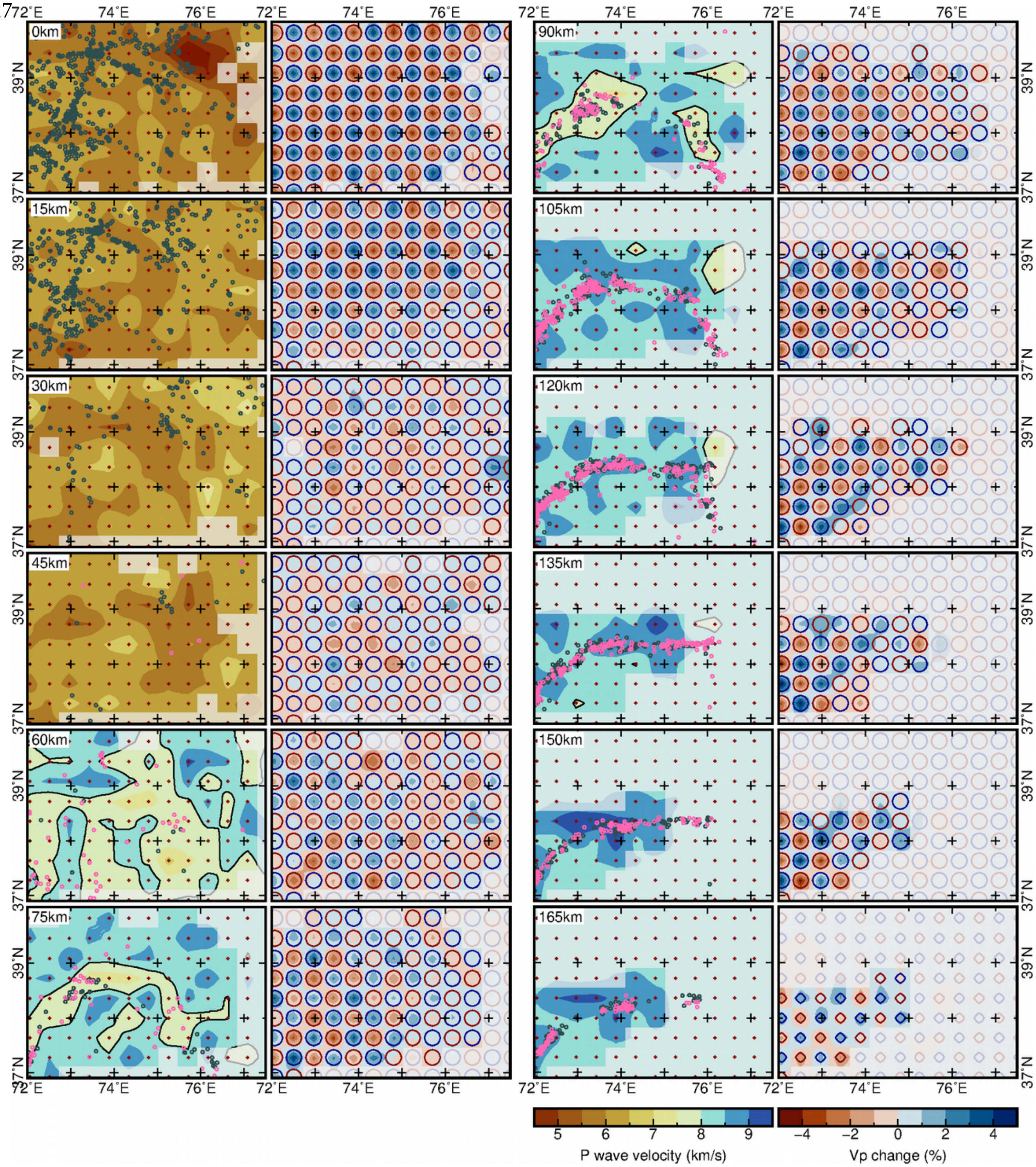

Figure S3: Horizontal slices through the tomogram at the node planes. Columns 1 and 3: Seismic velocities (colored background), grid nodes (red crosses), earthquakes used for tomographic inversion (gray circles), relocated earthquakes at intermediate depth (pink circles). Columns 2 and 4: Results of checkerboard recovery test: recovered model (colored background), input model (+/- 1% contours).

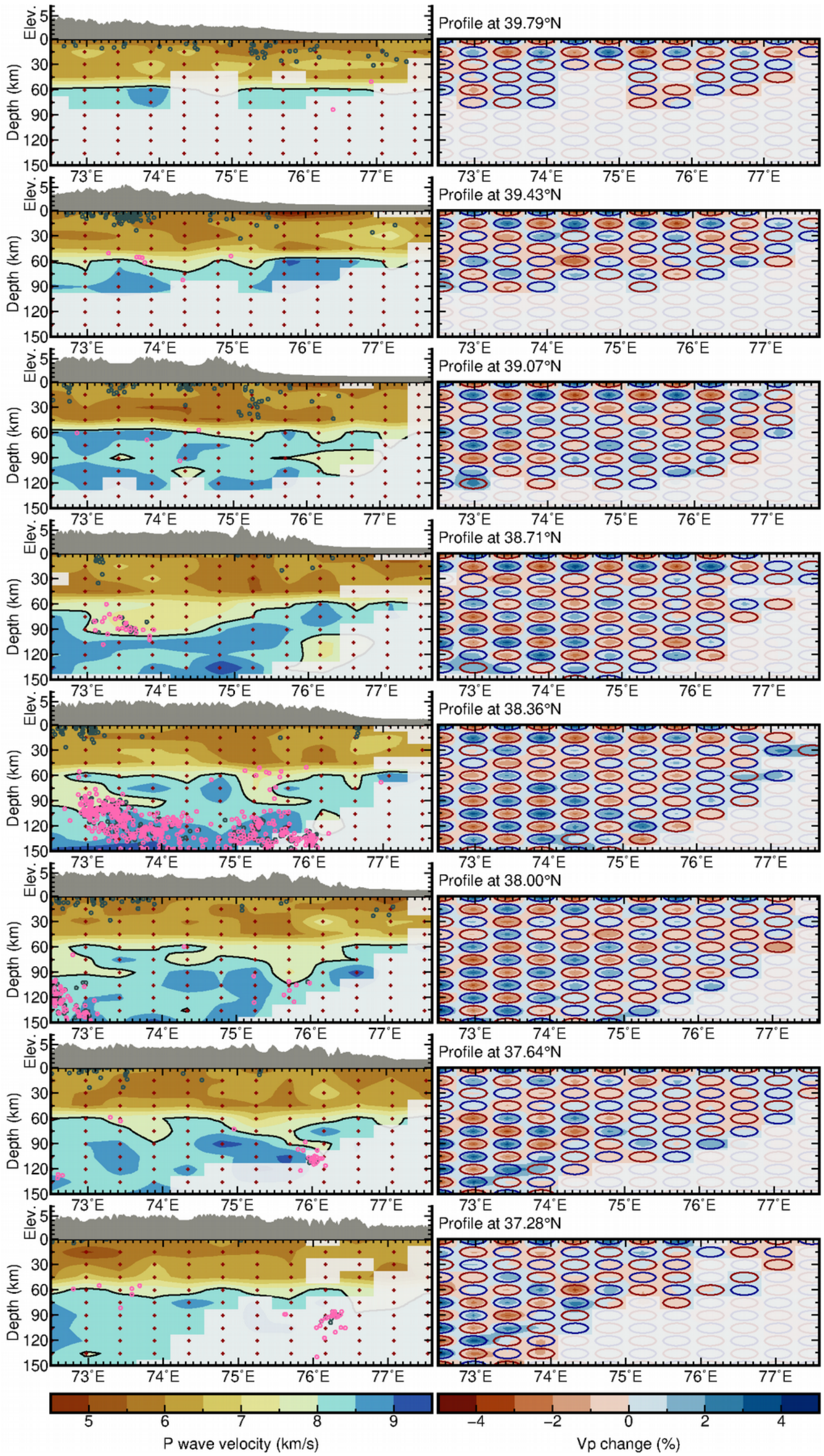

Figure S4: Same as Fig. S3, but with West-East-profiles.

129

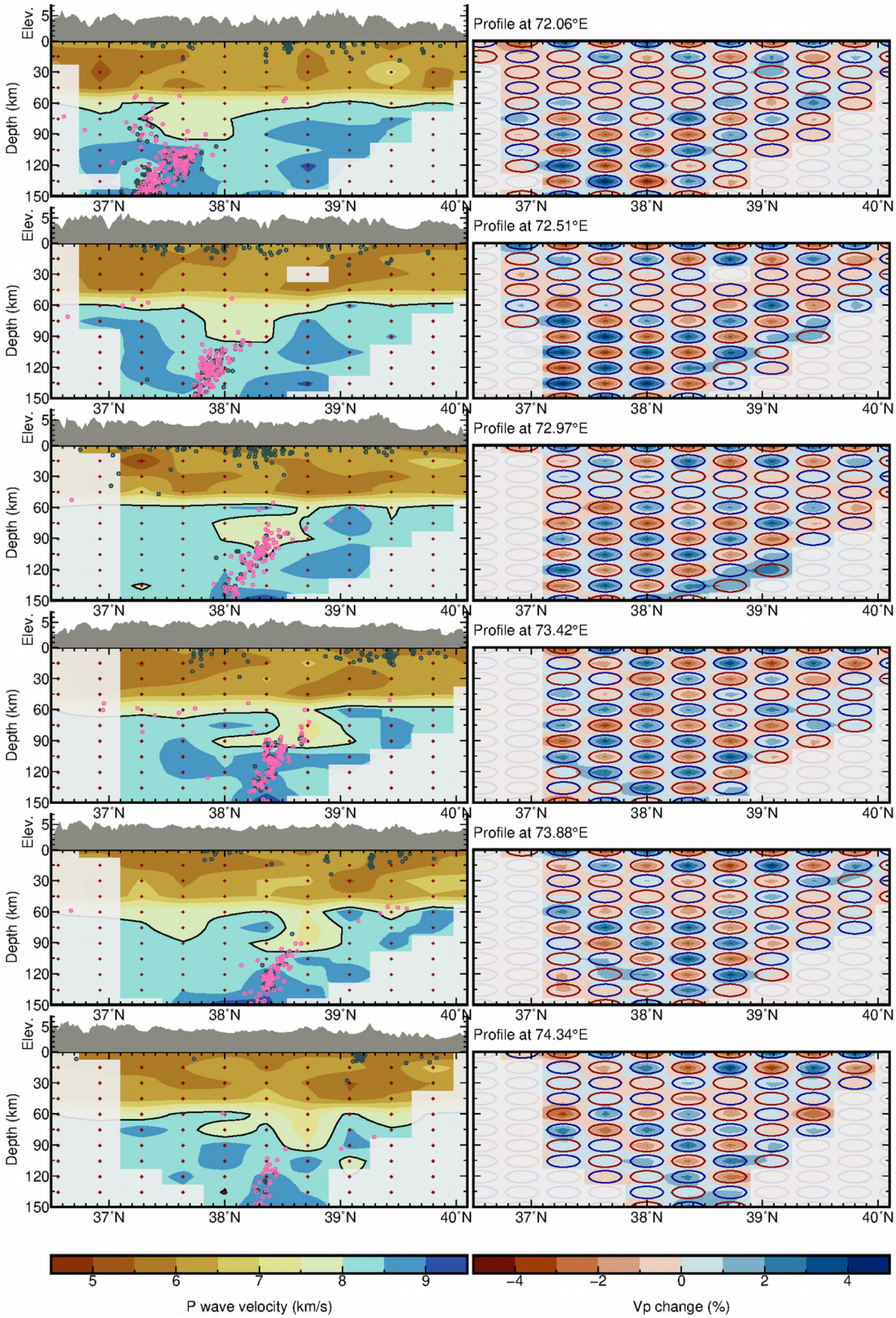

Figure S5: Same as Fig. S3, but with South-North-profiles.

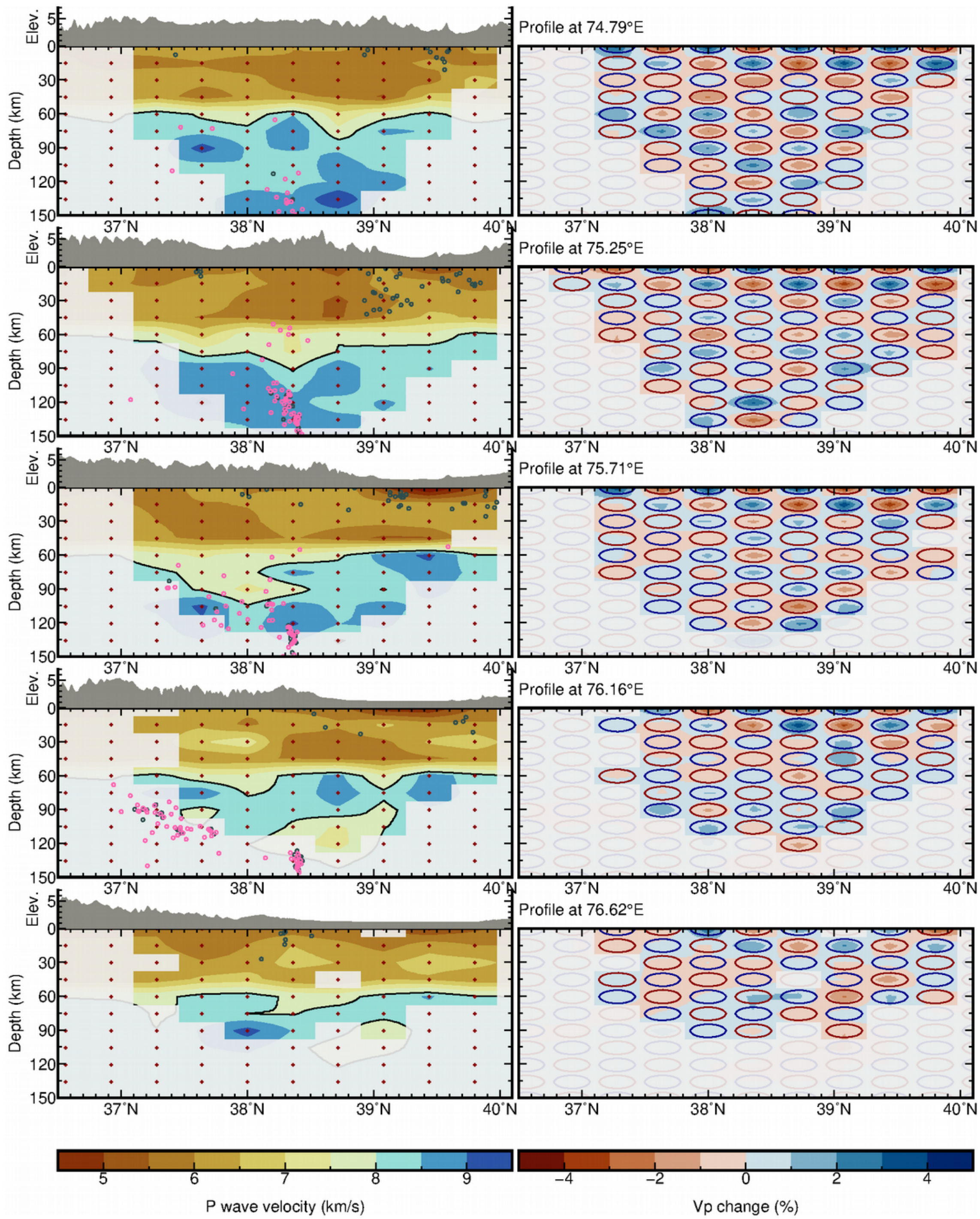

Figure S6: Fig. S5, continued

REFERENCES

Aldersons, F., 2004, Toward three-dimensional crustal structure of the Dead Sea region from local earthquake tomography [PhD thesis]: Tel-Aviv University.

Comino, J. Á. L., Heimann, S., Cesca, S. , Milkereit, C., Dahm, T. , and Zang, A., 2017, Automated full waveform detection and location algorithm of acoustic emissions from hydraulic fracturing experiment: Procedia engineering, v. 191, p. 697–702, doi:10.1016/j.proeng.2017.05.234.

Diehl, T., Deichmann, N., Kissling, E., and Husen, S., 2009, Automatic S-wave picker for local earthquake tomography. Bulletin of the Seismological Society of America, v. 99, p. 1906–1920, doi:10.1785/0120080019.

Gephart, J. W., and Forsyth, D. W., 1984, An improved method for determining the regional stress tensor using earthquake focal mechanism data: application to the San Fernando earthquake sequence: Journal of Geophysical Research: Solid Earth, v. 89, p. 9305–9320, doi:10.1029/JB089iB11p09305.

Hardebeck, J. L., and Shearer, P. M., 2003, Using S/P amplitude ratios to constrain the focal mechanisms of small earthquakes: Bulletin of the Seismological Society of America, v. 93, p. 2434–2444, doi:10.1785/0120020236.

Kissling, E., Ellsworth, W., Eberhart-Phillips, D., and Kradolfer, U., 1994, Initial reference models in local earthquake tomography. Journal of Geophysical Research: Solid Earth, v. 99, p. 19635–19646, doi:10.1029/93JB03138.

Lee, W. H. K., and Lahr, J. C., 1972, HYPO71: A computer program for determining hypocenter, magnitude, and first motion pattern of local earthquakes: US Department of the Interior, Geological Survey, National Center Earthquake Research

PMP International (Tajikistan), 2005, Tajikistan National Seismic Network. International Federation of Digital Seismograph Networks. doi:10.7914/SN/TJ.

SEISDMC, 2021, Data Management Centre of the China National Seismic Network at the Institute of Geophysics, China Earthquake Administration, doi:10.11998/SeisDmc/SN, (http://www.seisdmc.ac.cn/)

Sippl, C., Schurr, B., Yuan, X., Mechie, J., Schneider, F., Gadoev, M., Orunbaev, S., Oimahmadov, I., Haberland, C., Abdybachaev, U. et al., 2013a, Geometry of the Pamir-Hindu Kush intermediate-depth earthquake zone from local seismic data: Journal of Geophysical Research. Solid Earth, v. 118, p. 1438–1457, doi:10.1002/jgrb.50128.

Thurber, C. H., 1983, Earthquake locations and three-dimensional crustal structure in the Coyote Lake area, central California: Journal of Geophysical Research: Solid Earth, v. 88, p. 8226–8236.

Waldhauser, F., and Ellsworth, W. L., 2000, A double-difference earthquake location algorithm: Method and application to the northern Hayward fault, California: Bulletin of the Seismological Society of America, v. 90, p. 1353–1368, doi:10.1785/0120000006.

Yuan, X., Schurr, B., Bloch, W., Xu, Q., and Zhao, J., 2018a, East Pamir Network, GFZ Data Services, doi:10.14470/3U7560589977.

Yuan, X., B. Schurr, Kufner, S.-K., and Bloch, W., 2018b, Sarez Pamir aftershock seismic network, GFZ Data Services. doi:10.14470/4U7561589984.